JOURNAL OF PROPULSION AND POWER
Vol. 30, No. 1, January–February 2014

Effect of Magnetic Field Strength on a Magnetic Thrust Chamber System

Akihiro Maeno*
Kyushu University, Fukuoka 816-8580, Japan
Tomoyuki Hinaga† and Naoji Yamamoto‡
Kyushu University, Fukuoka 816-8508, Japan
Atsushi Sunahara§
Institute for Laser Technology, Osaka 565-0871, Japan
Shinsuke Fujioka¶
Osaka University, Osaka 565-0871, Japan
and
Hideki Nakasima**
Kyushu University, Fukuoka 816-8508, Japan

DOI: 10.2514/1.B34911

To confirm the validity of the modified numerical simulation performing a series of numerical simulations for high-energy laser injection onto a spherical target and the ablation plasma behavior in a magnetic field, the modified numerical simulation is compared with experiments and original numerical simulation. The modified numerical simulation consists of a one-dimensional Lagrangian radiation hydrodynamic code to calculate the creation process of laser-produced plasma and a three-dimensional hybrid particle-in-cell code. The original numerical simulation does not consider the creation process. The measured impulse bit due to the interaction between the diamagnetic current in a laser-produced plasma and the magnetic field generated by neodymium permanent magnets is 2.42 ± 0.23 μN · s. The calculated impulse bit in the modified and original numerical simulations is 10.3 and 72.7 μN · s, respectively. These results reveal that the modified numerical simulation models closer to the experiment than the original numerical simulation. In addition, to investigate the effect of the magnetic field strength on the plasma behavior in a magnetic thrust chamber system for a laser fusion rocket, the modified numerical simulation is performed. As a result, it is revealed that there is an approximation region of the magnetic field strength for high thrust performance.

Nomenclature

B	=	magnetic field
c	=	speed of light
c_{ve}	=	electronic specific heat
c_{vi}	=	ion specific heat
D_ν	=	diffusion coefficient for ν
e	=	elementary charge
E	=	electric field
E_ν	=	photon energy density for ν
j_i	=	ion current density
k_B	=	Boltzmann constant
m_e	=	electron mass
m_i	=	ion mass
N	=	number of ions
n_e	=	electron density
n_i	=	ion density
p_e	=	electron pressure
p_i	=	ion pressure
q	=	artificial viscosity
Q_e	=	electron source term
Q_i	=	ion source term
t	=	time
T_e	=	electron temperature
T_i	=	ion temperature
v	=	fluid velocity
v_e	=	electron velocity
v_i	=	ion velocity
Z	=	charge state of ion
Z^*	=	effective charge state of ion
α	=	thermal relaxation coefficient
η_ν	=	emissivity for ν
κ_e	=	electron thermal conductivity
κ_i	=	ion thermal conductivity
λ	=	laser wavelength
μ_0	=	permeability of vacuum
ν	=	frequency group
ν_{abs}	=	energy damping rate
ρ	=	mass density
τ_{ei}	=	equipartition time
χ_ν	=	absorption coefficient for ν

Received 14 January 2013; revision received 31 August 2013; accepted for publication 3 September 2013; published online 30 December 2013.

*Graduate Student, Interdisciplinary Graduate School of Engineering Science, Kasuga; maeno@aees.kyushu-u.ac.jp.
†Graduate Student, Interdisciplinary Graduate School of Engineering Science, Kasuga.
‡Associate Professor, Interdisciplinary Graduate School of Engineering Science, Kasuga.
§¶Researcher, Institute for Laser Technology, Suita.
¶Associate Professor, Institute of Laser Engineering, Suita.
**Professor, Interdisciplinary Graduate School of Engineering Science, Kasuga.

I. Introduction

IN THE future, space propulsion systems capable of generating large thrusts with high specific impulses will be required for manned interplanetary flights. A promising rocket is the laser fusion rocket (LFR), which was first proposed in the 1970s by Hyde et al. [1] and Hyde [2]. Orth et al. [3,4] estimated that an LFR employing a deuterium-tritium (DT) fusion reaction will have an effective specific impulse of 15,500 s and a thrust of 230 kN. Laser fusion means inertial confinement fusion (ICF) [5] that releases large amounts of

energy and creates high-energy-density plasma in about 10 ps by focusing homogenously laser beams onto a millimeter-sized capsule target filled with DT fuel. The laser pulse energy absorbed on the critical surface of the target generates an ablation plasma. This high-pressure plasma causes the fuel to implode to the center of the target. In this process, the target is compressed to a density several thousand times greater than that of solid materials. The DT fusion reaction, $D + T \rightarrow n(14.1\ MeV) + {}^4He(3.5\ MeV)$ releases about 400 MJ from a 2-mm-diam capsule target filled with DT fuel.

The LFR employs a magnetic thrust chamber system to generate thrust. The system produces thrust by inducing a diamagnetic current in the laser-produced plasma. Figure 1 depicts the mechanism for producing thrust in the system of an LFR. It involves the following processes:

1) ICF plasma expands in an applied magnetic field with a suitably designed geometry. The magnetic field is typically produced by a solenoid superconducting magnet (SCM).

2) Because plasmas are good conductors, the charged particles in the plasma undergo Larmor motion when a magnetic field is applied. This Larmor motion induces the diamagnetic current to sweep aside the magnetic field. Then, the magnetic field is compressed.

3) The compressed magnetic field pushes the plasma back in a manner similar to a spring. LFR then generates thrust through the interaction between the diamagnetic current in the plasma and the magnetic field generated by the SCM.

The magnetic thrust chamber system of an LFR has the following three advantages. First, it reduces the time of space missions because an LFR can generate large thrusts with high specific impulses. This will reduce the exposure of the space flight crew to cosmic radiation, which is one of the greatest problems associated with manned space flight. Second, the thrust can be easily varied during the mission by varying the system parameters. For example, the thrust can be changed by varying the operation frequency of the system because the thrust is proportional to the production frequency of impulse bits. Third, this system has a long lifetime. The direct plasma impingement on the solid wall of the vehicle is minimized as the plasma is confined by the magnetic field produced by the SCM, although the radiation shielding of the vehicle is damaged. Consequently, little charged plasma energy is wasted and the damage of the spacecraft structure is minimized, resulting in long lifetimes.

Several numerical simulations and experiments have been performed to investigate the behavior of the laser-produced plasma in the magnetic thrust chamber system for an LFR. In experiments, Vchivokv et al. [6] observed the temporal plasma behavior in an axially symmetric dipole magnetic field. Using a magnetic probe, they discovered that a diamagnetic cavity forms in the applied magnetic field. Maeno et al. [7,8] experimentally demonstrated a novel system for an LFR that employed a laser-produced plasma and cylindrical neodymium permanent magnets, rather than an ICF plasma and an SCM. These experiments for various laser pulse energies were performed using an extreme ultraviolet (EUV) database and the laser facilities at Gekko XII (GXII), in collaboration with Osaka University having these laser facilities made for researching EUV lithography and ICF. The impulse bit due to the interaction between the diamagnetic current in the plasma and the magnetic field generated by the magnets was directly measured by using a pendulum thrust stand. The impulse bits for the EUV database and the GXII laser facilities were in the ranges 1.5–2.5 $\mu N \cdot s$ and 0.03–10 $mN \cdot s$, respectively. In addition, no measurable impulse bit was observed when a nonmagnetized cylindrical iron was used instead of the magnets. These results indicate that the magnetic thrust chamber system for an LFR is capable of generating an impulse bit. They also show that the impulse bit increases with increasing laser pulse duration, laser pulse energy, an\d laser frequency (which is inversely proportional to the laser wavelength). In numerical simulations [9,10], a three-dimensional (3-D) hybrid particle-in-cell (PIC) code [11–13] was used to simulate the behavior of charged particles in a magnetic field.

Then, we tried to use only the 3-D hybrid PIC code (original code) to estimate the impulse bit measured in the previous experiment [7], in which the representative measured impulse bit is $2.42 \pm 0.23\ \mu N \cdot s$ at a laser pulse energy of 1.05 J and a laser pulse duration of 9 ns. Six cylindrical neodymium permanent magnets connected in the axial direction were used to generate a magnetic field. Each permanent magnet is 16 mm in diameter and 10 mm long. The permanent magnets were arranged so as not to disturb the incident laser beam. The distance between the axis of the permanent magnets and the target is 11 mm and the angle between the permanent magnets and the laser beam is 45 deg. The magnetic field strength at the target is calculated to be 0.12 T. In the original numerical simulation, the following initial plasma conditions were added to the code. The plasma mass is taken to be the target mass. The ion density is assumed to have a uniform distribution. The ion speed distribution is assumed to have a Maxwellian distribution and the initial plasma kinetic energy is assumed to be 30% of the incident laser pulse energy. The calculated impulse bit of $72.7\ \mu N \cdot s$ did not agree well with the measured value. This is considered to be because the input conditions do not account for the creation process of a laser-produced plasma. To consider the creation process in numerical simulations, Maeno et al. [14] performed a series of numerical simulations for the high-energy laser injection onto a spherical target and the ablation plasma behavior in a magnetic field. They combined a 3-D hybrid PIC code and a one-dimensional (1-D) Lagrangian radiation hydrodynamic code [15], which can compute the hydrodynamic evolution of a radiating plasma heated by laser pulses (modified code).

In the present study, to confirm the validity of the modified numerical simulation that considers the creation process of a laser-produced plasma, we compare results obtained using it with those obtained using the original numerical simulation that does not consider the creation process and with experimental results. Using these two numerical simulations, we investigate the effect of the magnetic field strength on the plasma behavior in a magnetic thrust chamber system for an LFR.

II. Numerical Simulation Methods

A. 1-D Lagrangian Radiation Hydrodynamic Code

A 1-D Lagrangian radiation hydrodynamic code named Star-1D was developed by Sunahara et al. [16]. Star-1D can simulate the evolution of a wide variety of high-energy-density laser-produced plasmas. It employs a one-fluid. In the high-density plasma, although the relative velocity between the nuclei is generated by the self-organized electromagnetic field, the nuclei collide with each other and comoving as one-fluid. On the other hand, because the temperature directly affect plasma pressure, the two-temperature ($T_i \neq T_e$) model is employed. The plasma is assumed to be quasi neutral due to comoving electrons (i.e., $Zn_i = n_e$). Thus, the following equations are solved. Equation (1) is the equation of continuity. Equation (2) is the equation of motion in planar and spherical geometries, in which the artificial viscosity q smooths the shock front. Equations (3) and (4) are energy equations for ions and electrons, respectively

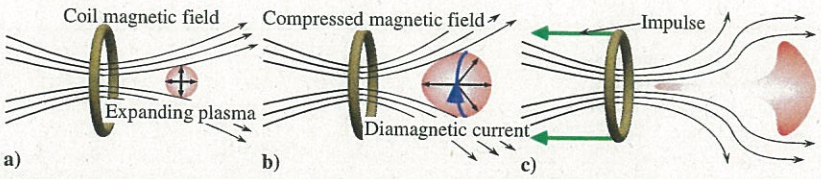

Fig. 1 Mechanism for generating thrust in the magnetic thrust chamber system of an LFR. The LFR produces thrust through the interaction between the diamagnetic current and the magnetic field.

$$\frac{d\rho}{dt} + \rho\nabla \cdot v = 0 \tag{1}$$

$$\frac{dv}{dt} = -\frac{1}{\rho}\nabla(p_i + p_e + q) \tag{2}$$

$$\rho c_{vi}\frac{dT_i}{dt} = -p_{THi}\nabla \cdot v + \nabla \cdot (\kappa_i \nabla T_i) + \alpha(T_e - T_i) + Q_i \tag{3}$$

$$\rho c_{ve}\frac{dT_e}{dt} = -p_{THe}\nabla \cdot v + \nabla \cdot (\kappa_e \nabla T_e) - \alpha(T_e - T_i) + Q_e \tag{4}$$

$$p_{THs} = T_s\left(\frac{\partial p_s}{\partial T_s}\right)_\rho \tag{5}$$

In Eqs. (2–5), the variables p_s, c_{vs}, and p_{THs} are functions of n_i and T_s. They are obtained from SESAME equation of state tables [17]. Here, the subscript s indicates an ion (i) or an electron (e). The second terms on the right-hand sides of Eqs. (3) and (4) represent thermal conduction due to ions [18] and electrons [19], as shown in Eq. (6). Here, Z^* is defined as $< Z^2 > / < Z >$, where $< >$ indicates averaging over the ion species, and ln Λ is Coulomb logarithm [20]. The flux-limited Spitzer–Harm model [21], with a flux limit factor of 0.1, is applied. The third terms in Eqs. (3) and (4) indicate electron-ion temperature relaxation. Here, $\alpha(= 1.5k_B n_e/f\tau_{ei})$ is determined from the Spitzer relaxation time [22], as shown in Eq. (7), and f is the reduction factor of the laser absorption due to the Langdon effect [23], which is important for long-wavelength laser irradiation. Here, $Q_i(= -q\nabla \cdot v)$ is the viscous heat, which is generated by the conversion of kinetic energy into ion thermal energy due to the viscosity. Here, Q_e consists of a laser energy deposition term and a laser heating term for electrons. The laser energy deposited between the vacuum-plasma boundary (expansion surface) and the critical surface is calculated by ray tracing using 100 rays. The critical surface density $n_{cr}(= 4\pi m_e/\mu_0 e^2\lambda^2)$ is 9.8×10^{20} cm^{-3}. The laser absorption coefficient [24] is denoted by ν_{abs}/v_g. Inverse bremsstrahlung [25] is assumed to occur during the laser energy absorption process. Other mechanisms, such as resonance and parametric absorptions, are not considered because they mostly convert the light energy to the energy of the plasma waves and produce superthermal electrons. In general, such mechanisms do not cause local thermalization on the critical surface. The deposition for each calculation mesh is calculated to be $P = \exp(-\nu_{abs}\Delta t)$, as shown in Eq. (8), where P is the local laser power, and Δt is the time taken for the laser ray to pass through each mesh size at its group velocity ($v_g = c\sqrt{1 - (n_e/n_{cr})^2}$)

$$\kappa_i = \frac{2.925(k_B T_i)^{5/2}}{\sqrt{\pi m_i} e^4 < Z^2 >^2 \ln \Lambda_{ii}}$$

$$\kappa_e = \frac{16\sqrt{2}(k_B T_e)^{5/2}}{\phi\pi^{5/2}\sqrt{m_e} e^4 Z^* \ln \Lambda_{ei}},$$

$$\phi = \frac{Z^* + 4.2}{Z^* + 0.24} \tag{6}$$

$$\tau_{ei} = 1/\frac{8\sqrt{2\pi m_e} e^4 n_i < Z^2 > \ln \Lambda_{ei}}{3m_i(k_B T_e)^{3/2}} \tag{7}$$

$$\nu_{abs} = \frac{4\sqrt{2m_e}\pi^{3/2} c^2 e^2 Z^* \ln \Lambda}{3\lambda^2 (k_B T_e)^{3/2}}\left(\frac{n_e}{n_{cr}}\right)^2 \tag{8}$$

Equation (9) is the radiative transport equation. To evaluate the radiation transport process, the multigroup diffusion approximation model [26] using a flux limit, as shown in Eq. (10), is applied. The photon energy $h\nu$ is in the range 0–1 keV; this range is divided into 100 bins for ν to numerically solve Eq. (9), where h is the Planck constant. Here, $h\nu$ and the opacity $\kappa_\nu(= \chi_\nu/\rho)$ are based on the collisional radiative equilibrium model. In this model, the plasma is assumed to be optically thin without reabsorption of the radiation energy

$$\rho\frac{d}{dt}\left(\frac{E_\nu}{\rho}\right) + \nabla \cdot (D_\nu \nabla E_\nu) = 4\pi\eta_\nu - c\chi_\nu E_\nu \tag{9}$$

$$D_\nu = -\frac{c}{3\chi_\nu + |\nabla E_\nu|/E_\nu} \tag{10}$$

B. 3-D Hybrid PIC Code

Nagamine and Nakashima [9] developed a 3-D hybrid PIC code to simulate plasma behavior in a magnetic field. This code treats ions as individual particles and electrons as a magnetic hydrodynamic fluid. The basic equations are given next. Equations (11) and (12) are the equations for particle and fluid motion, respectively. Here, m_e is assumed to be zero because the code neglects the inertial term. High-frequency plasma phenomena, the resistivity, and electron motions, such as electron plasma oscillation and cyclotron motion, are also neglected [27]. The plasma is assumed to be quasi neutral due to comoving electrons (i.e., $Zn_i = n_e$). Here, T_e is assumed to be zero because the plasma cools as it expands and its inertial energy will be converted into kinetic energy. Here, p_e is also assumed to be zero from $p_e = n_e k_B T_e$. Equation (13) is given by Ampere's law and $j_i = Zen_i v_i$. The transverse displacement current in Ampere's law is neglected by the Darwin approximation. The ion current density is important because it relates the ion motion to the electromagnetic field. These approaches are valid because the system behavior is dominated by ion physics

$$n_i m_i \frac{dv_i}{dt} = Zen_i(E + v_i \times B) \tag{11}$$

$$n_e m_e \frac{dv_e}{dt} = -en_e(E + v_e \times B) - \nabla p_e \tag{12}$$

$$v_e = \frac{1}{en_e}\left(j_i - \frac{\nabla \times B}{\mu_0}\right) \tag{13}$$

C. Coupling Procedure Between Two Codes

In the modified numerical simulation, the results of Star-1D are used as 3-D ion super particle distributions for the particle position and expansion velocity, which are inputted into the 3-D hybrid PIC code. To convert from a 1-D Lagrangian mesh model to a 3-D Cartesian coordinate particle model, the plasma is assumed to expand into the vacuum isotropically as the 1-D meshes are elements along the radius of multilayer sphere. Because the number of ions in each shell is calculated by multiplying the shell volume by the ion density, it is easy to divide the ion superparticles into each shell. Finally, the physical quantities of the 1-D meshes are distributed among the ion superparticles. When the number of ion superparticles is small by the limitation of calculation cost, the number of particles divided into the outer shells is few because the ion density of the outer shells is smaller than that of the inner shells by a few orders of magnitude.

The inputted ions have only expansion velocities; they do not have thermal velocities. The effect of ion thermal velocity is negligibly small because the ion expansion velocity accelerated by the laser is faster than the thermal velocity estimated from the ion temperature.

III. Experiment Method

A. Experimental Setup

In the experiment setup, shown in Fig. 2, the ion beam current of a laser-produced plasma was first measured using a charge collector. The distance between the charge collector and the origin is 155 mm and the angle between the charge collector and a single laser beam is 14 deg. The plasma was created by focusing a 1064 nm Nd:YAG laser beam (pulse duration: 9 ns; pulse energy: 4 J) onto a 500-μm-diam spherical polystyrene target. The laser beam was focused on the central axis of the coil by a lens (F-number: 20) so that its diameter was equal to that of the target. To reduce the measurement error caused by the ablation plasma generated by the glass rod, the target was suspended on the end of a carbon fiber attached to a glass rod. A pulsed power supply and an edgewise coil were used to generate a pulsed magnetic field. The coil (outer diameter: 60 mm; inner diameter: 50 mm; length: 10 mm) that generates the magnetic field consists of 10 turns of a rectangular copper wire. The wire is coated with a polyimide thin film as an insulator (width: 5 mm; thickness perpendicular to the coil axis: 1 mm). The coil is set 25 mm from the origin, as shown in Fig. 2. The edgewise coil has a high lamination factor, a small temperature difference between the inside and outside of the coil, and a high-frequency response.

B. Charge Collector

Figure 3 shows the charge collector that consists of a Faraday cup [28] and the current-to-voltage (I–V) converter. The charge collector in the vacuum chamber is biased to −50 V to repel electrons. Four resistors with a resistance of 50 Ω each are used for impedance matching. The Faraday cup has a very low secondary electron emission rate, making it very suitable for absolute measurements of the ion number and energy. This is because almost none of the secondary electrons generated in the Faraday cup escape from the collector through the 4-mm-diam hole, as shown in Fig. 3. To prevent electrons in the plasma from entering the Faraday cup, the hole is covered with a mesh that has 500 lines/in. with a line diameter of 0.025 mm and an ion penetration rate of 25%. The ion expansion velocities were derived by dividing the distance between the target and this probe (155 mm) by the arrival time of ion beam current.

C. Pulsed Power Supply

The pulsed power supply was made by us and uses a three-step pulse forming network (PFN) [29]. The power supply can generate a maximum current of 10 kA with a pulse width of 20 μs when the charging voltage is 5 kV. The circuit diagram of the supply is shown in Fig. 4. The section of the PFN that supplies a voltage consists of a high-voltage dc power supply, a switch, a charging resistor (100 kΩ), and a potential divider (1 GΩ and 1 MΩ). The section for the charging voltage consists of three capacitors (32 μF), two inductors (2 μH), a matching resistor (250 mΩ), a fast high-voltage solid-state diode, and a switch. The edgewise coil in the vacuum chamber has a self-inductance of 7 μH. Figure 5 shows the experimental and theoretical output currents of this supply when measuring a potential drop across a 0.002 mΩ current shunt resistor for a charging voltage

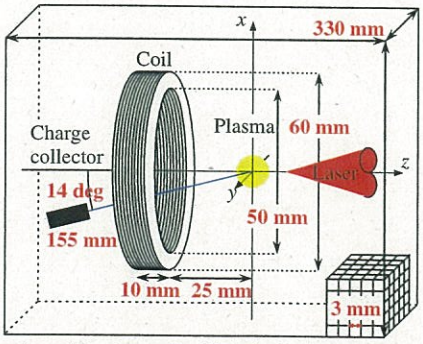

Fig. 2 Experimental setup and cubic calculation model for 3-D hybrid PIC code.

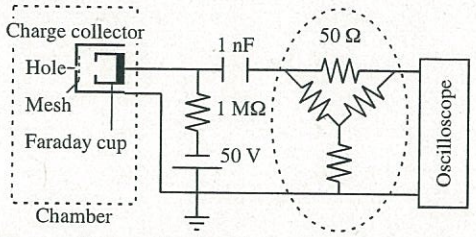

Fig. 3 Charge collector with a Faraday cup and an I–V converter. The 4-mm-diam hole is covered with a mesh to prevent electrons in the plasma from entering the Faraday cup.

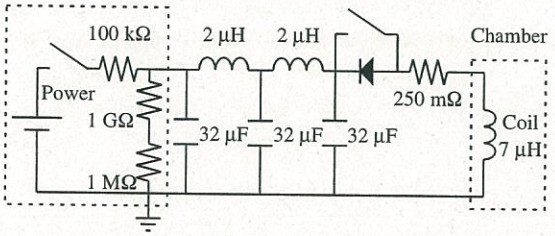

Fig. 4 Circuit diagram of pulsed power supply with a three-step PFN.

of 230 V. The peak current is 450 A at 10 μs. The current starts to flow 31 μs prior to laser ignition induced by a digital delay/pulse generator. The monitored current agrees well with the theoretical value.

D. Torsional Thrust Stand

In the previous experiment, some impulse bits due to the interaction between the diamagnetic current and the magnetic field were measured under the certain condition of the magnetic field strength of 0.12 T. In this experiment, the impulse bit measurement was tried by using a torsional thrust stand that has a detection limit of 50 μN · s. The stand is calibrated by striking the thrust stand to cause an impact. The impact is directly measured by a force transducer attached to the counterweight. The force transducer records the impulsive force as a function of time; integrating this yields the applied impulse. It is assumed that the impulse on the force transducer is proportional to the amplitude of the output of the stand. It is also verified that the output is zero when the pulsed magnetic field of the edgewise coil is generated without plasma. However, the level of the impulse bit was lower than the detection limit of the thrust stand.

IV. Numerical Simulation Conditions

A. Calculation Model of Star-1D

To compute the experiment using a carbon–hydrogen (CH) spherical target with a diameter of 500 μm, the target is divided into six parts. Each part has a solid angle of 0.636 π sr, as shown in Fig. 6. In the experiment, a single laser beam is focused onto the target. In

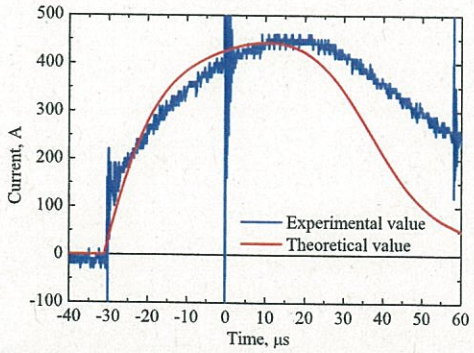

Fig. 5 Experimental and theoretical output currents of pulsed power supply at the peak current of 450 A. Current starts flowing 31 μs prior to laser ignition.

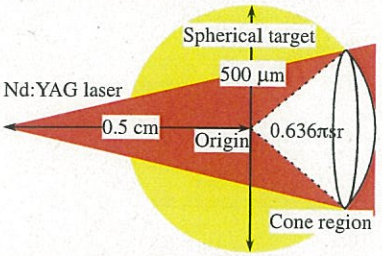

Fig. 6 Calculation model of Star-1D.

contrast, a single laser beam is assumed to be focused onto each part in Star-1D. The surface area of the part in Star-1D is assumed to be equal to the laser beam spot size (i.e., the full width at half maximum of the laser beam). Each laser beam has an energy of 0.636 J; i.e., the total energy of the laser beams focused onto the target is about 4 J. The laser beam is generated by a 1064 nm Nd:YAG laser with a Gaussian intensity profile. Figure 7 shows the Gaussian time-variable power profile of the laser beam. The rise and fall times of the peak power are 10 and 20 ns, respectively. The peak power of the laser beam is 2.51×10^8 W at the calculation time of 25 ns. The distance between the laser focal point and the target is set to 0.5 cm. The number of radial meshes with widths Δx in the range 0.01–1 μm is 500. They move with the hydrodynamic evolution of the plasma heated by the laser beam. For a CH material, the atomic mass averaged over carbon and hydrogen and the mass density are assumed to be 6.5 amu and 1.06 g/cm^3, respectively. The calculation start and finish times are set to 0 and 75 ns, respectively. The calculation time step Δt is initially set to 0.1 ps and it is subsequently varied according to the Courant–Friedrichs–Lewy (CFL) condition. When the numerical simulation does not meet the CFL condition ($c\Delta t/\Delta x < 1$), the numerical simulation becomes unstable and diverges.

B. Calculation Model of 3-D Hybrid PIC Code

The initial laser-produced plasma is located at the origin of the model. The model is an $110\Delta x \times 110\Delta x \times 110\Delta x$ cube, where $\Delta x =$ 3 mm is the mesh width, as shown in Fig. 2. Figure 8 shows the magnetic field strength along the central axis of z at $x = y = 0$ and in the z-x plane at $y = 0$, produced by the edgewise coil at the peak current of 450 A. The magnetic field strength at the origin is 0.0321 T. The calculation start time is set to zero. At this time, numerical simulations are changed from Star-1D to the 3-D hybrid PIC code. The number of ion superparticles is 10^6. To analyze the particle behavior in the electromagnetic field, a large number of particles is required. The calculation time is $100,000\,\Delta t$ (5 μs), where $\Delta t =$ 50 ps (ion cyclotron frequency $\omega_{ci} = 1/2047\Delta t$) is the time step. It is according to the CFL condition that c is replaced by the Alfven speed, because the hybrid PIC code uses the implicit method, not the explicit method.

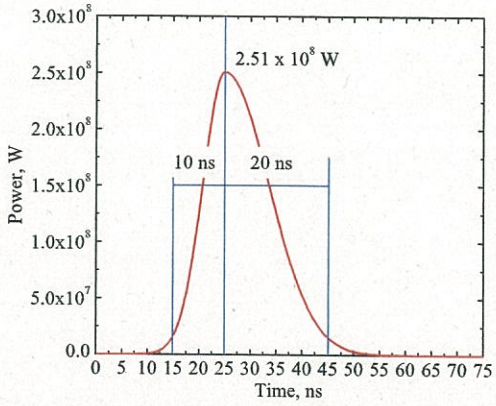

Fig. 7 Gaussian time-variable power profile of a single laser beam for Star-1D.

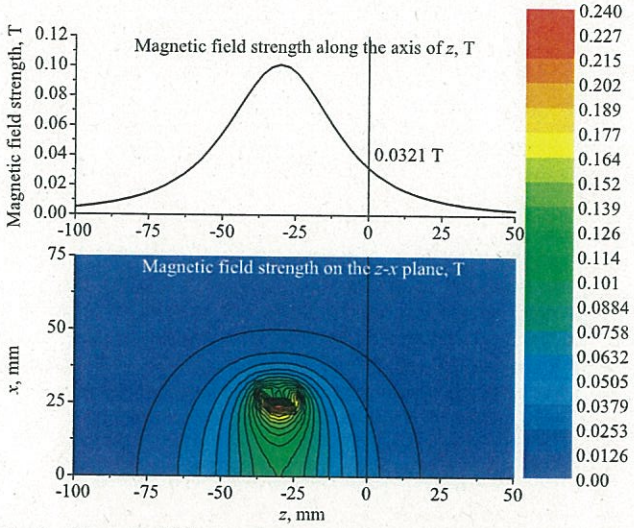

Fig. 8 Magnetic field strength produced by the edgewise coil at the peak current of 450 A. Magnetic field strength at the origin is 0.0321 T.

V. Results and Discussion

A. Impulse Bit and Ion Expansion Velocity in the Numerical Simulations and Experiments

We compare an impulse bit measured in a previous experiment [7] with the values computed by the modified numerical simulation to confirm the validity of the modified numerical simulation. The modified numerical simulation employing a 3-D hybrid PIC code and Star-1D, which accounts for the creation process of a laser-produced plasma, calculated the impulse bit as 10.3 μN · s. This does not agree with the value of the previous experiment [7] (2.42 ± 0.23 μN · s). This discrepancy is considered to be due to the calculation processes in Star-1D and the 3-D hybrid PIC code. Star-1D assumes that the plasma expands isotropically. In the experiments, the laser beam is focused on a section of the target face, whereas the laser beams are focused on almost the entire face of the target in Star-1D. This difference may affect the plasma mass and the expansion direction calculated by Star-1D. Another possible cause of the preceding discrepancy is the boundary between the plasma and vacuum in the 3-D hybrid PIC code. An ion density of 10^{16} cm^{-3} is used as the threshold for separating the plasma from the vacuum when calculating the electric field for the present conditions. When the desired level is smaller than the threshold, the 3-D hybrid PIC code diverges. Thus, having the electric field calculated in a vacuum rather than in a low-density plasma may affect the impulse bit. Another possible cause for the discrepancy is particle collisions. Collisions may reduce the impulse bit, but the 3-D hybrid PIC code assumes that the plasma is collisionless. However, the value for the impulse bit calculated by the modified numerical simulation is closer to that of the previous experiment than that of the original numerical simulation.

In this experiment, the measured ion expansion velocity at $B =$ 0.0321 T is 199 km/s. The uncertainty in the time range at the oscilloscope is of the order of nanoseconds, so that the uncertainty in the estimated velocity is negligible. In the original numerical simulation, the velocity is calculated to be: 15 km/s. The velocity obtained using the modified numerical simulation is 194 km/s. Thus, the experimentally measured velocity and that calculated by the modified numerical simulation at $B = 0.0321$ T are almost the same; that is, the initial plasma velocity for the modified numerical simulations is adequate for the experiment.

These indicate that the creation process of a laser-produced plasma is important when investigating plasma behavior in a magnetic field by numerical simulations. This is considered to be because the different ion expansion velocities calculated by the two numerical simulations affect the impulse bit.

Table 1 Ion expansion velocity calculated by the modified numerical simulation

Magnetic field strength, T	Ion expansion velocity, km/s
0.0321	194
0.961	194
1.92	182
2.88	155

B. Thrust Performance for Various Magnetic Field Strengths

The reason we were unable to measure an impulse bit in the experiment is considered to be that the ion expansion velocity of the plasma is very high, up to about 200 km/s. The high-speed ions pass through the system prior to interacting sufficiently with the magnetic field to be pushed back by the compressed magnetic field. If the magnetic field strength is sufficiently strong, the impulse bit should be high. The modified numerical simulation was used to investigate the effect of the magnetic field strength on the plasma behavior in the magnetic thrust chamber of an LFR. Calculations were conducted for magnetic field strengths at the origin of 0.0321, 0.961, 1.92, and 2.88 T.

Table 1 lists the ion expansion velocities in these four magnetic fields calculated by the modified numerical simulation. It is found that the ion expansion velocity decreases with increasing magnetic field strength from the value of 0.961 T. This indicates that, with increasing magnetic field strength, the plasma is decelerated more by the magnetic pressure when the plasma particles pass through the edgewise coil. Figures 9–12 show the ion super particle distributions at a calculation time of 5 μs in the z-x plane at $y = 0$ for various magnetic fields calculated by the two numerical simulations. They show the effect of the magnetic field strength in the magnetic thrust chamber of an LFR. The squares in the figures indicate the edgewise coil. When an ion super particle collides with the coil, the particle is eliminated from the 3-D hybrid PIC code. The particles with velocities of: 194 km/s expand isotropically into the vacuum, as shown in Fig. 9a. The plasma around the coil at $B = 0.961$ T (see Fig. 10a) is pushed back by the magnetic field. Figures 10a, 11a, and 12a show that the particle distribution changes with increasing magnetic field strength; specifically, the particles move in the exhaust direction without isotropically expanding at high magnetic field strengths. Therefore, the thrust of the system is improved by increasing the magnetic field strength. Figure 9b shows that the ions are guided by the magnetic field through the edgewise coil. In this case, the critical magnetic field strength is considered to be 0.961 T. That is, the particle distribution at $B = 0.961$ T shown in Fig. 10b is similar to the results for $B = 1.92$ T shown in Fig. 11b, and for $B = 2.88$ T shown in Fig. 12b. This suggests that thrust performance calculated by the original numerical simulation will saturate at magnetic field strengths greater than the critical magnetic field strength of $B = 0.961$ T. Figure 13 shows the impulse bits calculated by the modified and original numerical simulations. As the ion super particle distributions in Figs. 9–12 show, the impulse bit in the modified numerical simulation increases with increasing magnetic field strength from the value of 0.961 T, whereas the impulse bit in the original numerical simulation saturates at high magnetic field strengths.

From these results, when the effect of the magnetic field strength becomes larger as the ion expansion velocity is decelerated, the impulse bit increases. The effect on the thrust performance is small

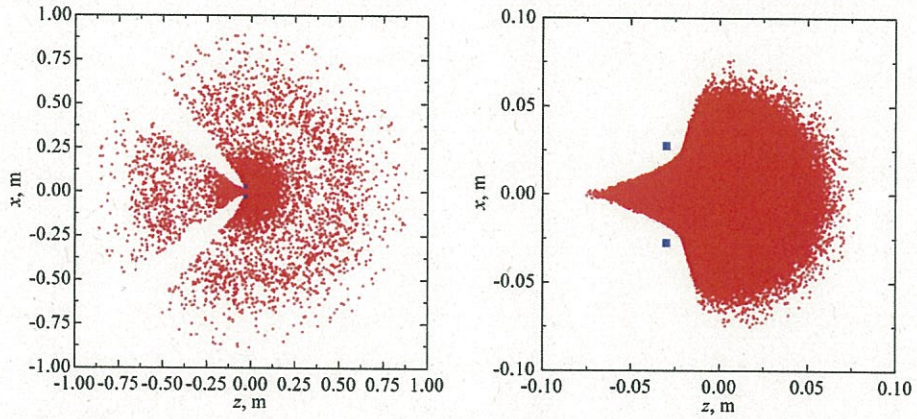

a) Modified **b) Original**

Fig. 9 Ion super particle distributions at $B = 0.0321$ T calculated by a) modified and b) original numerical simulations.

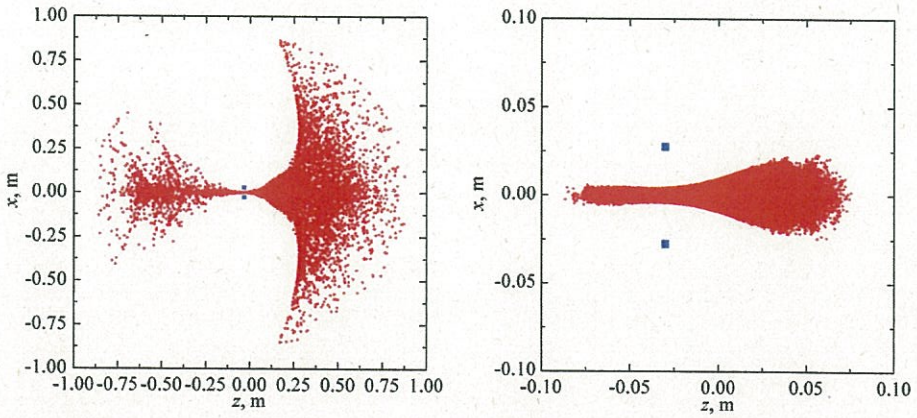

a) Modified **b) Original**

Fig. 10 Ion super particle distributions at $B = 0.961$ T calculated by a) modified and b) original numerical simulations.

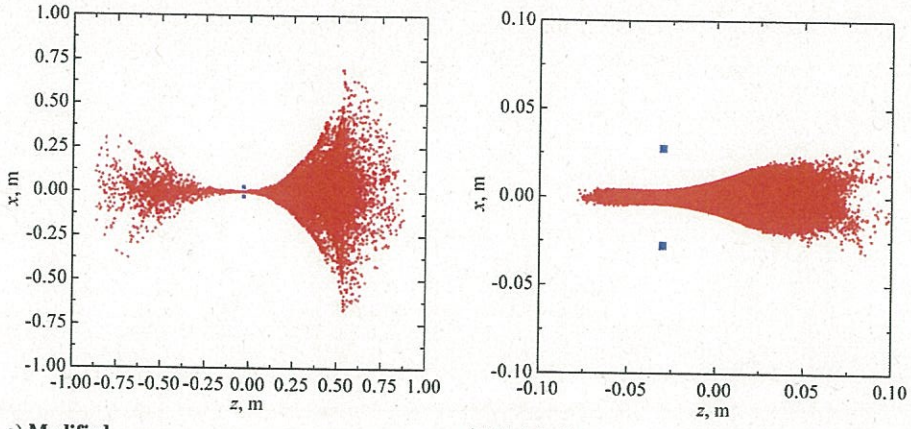

a) Modified b) Original

Fig. 11 Ion super particle distributions at $B = 1.192$ T calculated by a) modified and b) original numerical simulations.

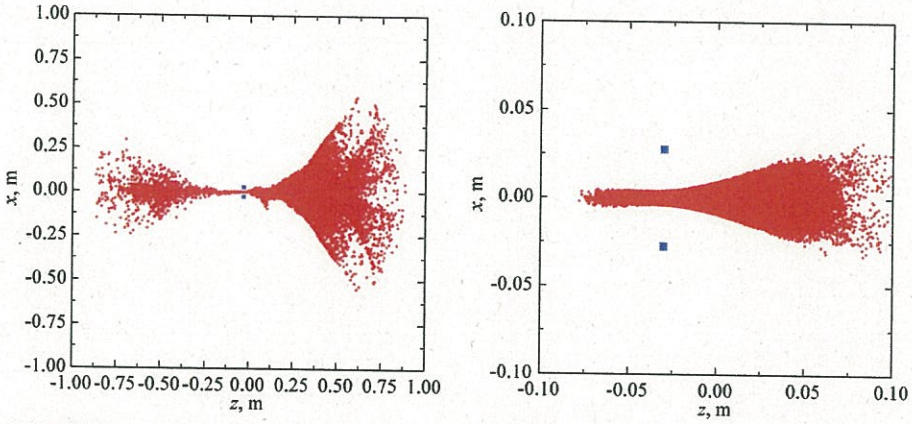

a) Modified b) Original

Fig. 12 Ion super particle distributions at $B = 2.88$ T calculated by a) modified and b) original numerical simulations.

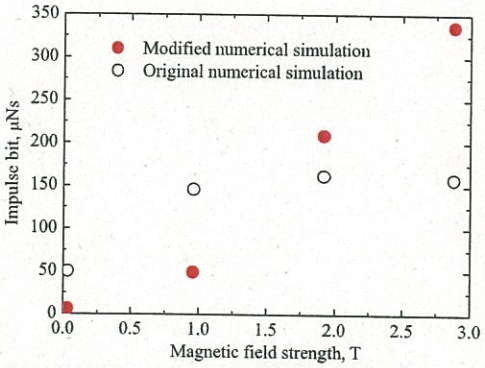

Fig. 13 Impulse bit for various magnetic field strengths calculated by modified and original numerical simulations.

when the magnetic field energy is much weaker than the threshold of 0.961 T. Thus, for high thrust performance, these results indicate that there is an approximation region of the magnetic field strength.

VI. Conclusions

A modified numerical simulation that uses Star-1D to calculate the creation process of a laser-produced plasma and a 3-D hybrid PIC code was used to perform a series of numerical simulations for high-energy laser injection onto a spherical target to investigate the ablation plasma behavior in a magnetic field. To confirm the validity of the modified numerical simulation, the results obtained using the modified numerical simulations were compared with those of experiments and the original numerical simulation (a 3-D hybrid PIC code that does not consider the creation process). Comparison of the impulse bit due to the interaction between the diamagnetic current in a laser-produced plasma and the magnetic field revealed that the modified numerical simulation is closer to the previous experiment than the original numerical simulation. Comparison of the ion expansion velocities measured by the charge collector and calculated by the two numerical simulations revealed that the experiment and the modified numerical simulation at $B = 0.0321$ T give almost the same ion expansion velocities. These results indicate that the creation process of a laser-produced plasma is important when investigating plasma behavior in a magnetic thrust chamber system for an LFR.

However, the impulse bit could not be measured in the final experiment because it was lower than the detection limit of the thrust stand. If the magnetic field strength is sufficiently high relative to high-speed ions, with velocities up to about 200 km/s, the impulse bit should increase. To investigate the effect of the magnetic field strength on the plasma behavior in a magnetic thrust chamber system for an LFR, modified numerical simulations were conducted for various magnetic field strengths. Calculations of the ion expansion velocity reveal that ions moving in the direction opposite to the exhaust direction through the edgewise coil are decelerated upon increasing the magnetic field strength. Calculations of the impulse bit reveal that the impulse bit increases with increasing magnetic field strength. Thus, for high thrust performance, it is found that there is an approximation region of the magnetic field strength.

In summary, the creation process of a laser-produced plasma significantly affects the plasma behavior in a magnetic thrust chamber system for an LFR. In the future, to estimate the optimal

experimental conditions, we plan to improve the modified numerical simulation by combining two-dimensional radiation hydrodynamic code instead of Star-1D and comparing with more experimental results. In addition, we would like to use the DT reaction calculation adjusted to radiation hydrodynamic code and to investigate an actual LFR.

Acknowledgments

This work was supported by the Japan Society of the Promotion of Science (JSPS) KAKENHI (Grants-in-Aid for Scientific Research) (grant number: 21360418) and a Grant-in-Aid for JSPS Fellows from the JSPS (number 22-1672). This work was performed in collaboration with the Institute of Laser Engineering, Osaka University, A1-42 and B1-38, 2011. We express our gratitude to Eiji Sato at Osaka University, Yoshitaka Mori at the Graduate School for the Creation of New Photonics Industries, Tomoyuki Johzaki at Hiroshima University, and Yoshihiro Kajimura at Akashi National College of Technology for their helpful assistance.

References

[1] Hyde, R. A., Wood, L. L., and Nuckolls, J. H., "Prospects for Rocket Propulsion with Laser-Induced Fusion Microexplosions," AIAA Paper 1972-1063, 1972.

[2] Hyde, R. A., "A Laser Fusion Rocket for Interplanetary Propulsion," Lawrence Livermore National Lab., UCRL-88857, Livermore, CA, 1983, p. 13.

[3] Orth, C. D., Klein, G., Sercel, J., Hoffman, N., Murray, K., and Chang-Diaz, F., "Transport Vehicle for Manned Mars Missions Powered by Inertial Confinement Fusion," Lawrence Livermore National Lab., UCRL-96832, Livermore, CA, 1987, p. 10.

[4] Orth, C. D., "VISTA—A Vehicle for Interplanetary Space Transport Application Powered by Inertial Confinement Fusion," *Introduction*, Lawrence Livermore National Lab., University of California, UCRL-LR-110500, Livermore, CA, 2003, pp. 2–11, Chap. 1.

[5] McCracken, G., and Stott, P., *Fusion: The Energy of the Universe*, 1st ed., Academic Press, Massachusetts, 2005, pp. 69–86, Chap. 7.

[6] Vchivokv, K. V., Nakashima, H., Zakharov, Y. P., Esaki, T., Kawano, T., and Muranaka, T., "Laser-Produced Plasma Experiments and Particle in Cell Simulation to Study Thrust Conversion Processes in a Laser Fusion Rocket," *Japanese Journal of Applied Physics*, Vol. 42, 2003, pp. 6590–6597.
doi:10.1143/JJAP.42.6590

[7] Maeno, A., Yamamoto, N., Nakashima, H., Fujioka, S., Mori, Y., Sunahara, A., and Johzaki, T., "Direct Measurement of the Impulse in a Magnetic Thrust Chamber System for Laser Fusion Rocket," *Applied Physical Letters*, Vol. 99, No. 7, 2011, pp. 1–3.
doi:10.1063/1.3626600

[8] Maeno, A., Yamamoto, N., Fujioka, S., Mori, Y., Sunahara, A., Johzaki, T., and Nakashima, H., "Analysis of Laser Wavelength and Energy Dependences of the Impulse in a Magnetic Thrust Chamber System for a Laser Fusion Rocket," *Transactions of the Japan Society for Aeronautical and Space Sciences*, Vol. 56, No. 3, 2013, pp. 170–172.
doi:10.2322/tjsass.56.170

[9] Nagamine, Y., and Nakashima, H., "Analysis of Plasma Behavior in a Magnetic Thrust Chamber of a Laser Fusion Rocket," *Fusion Science and Technology*, Vol. 35, No. 1, 1999, pp. 62–70.

[10] Kawabuchi, R., Matsuda, N., Kajimura, Y., Nakashima, H., and Zakharov, Y. P., "Numerical Simulation of Plasma Detachment from a Magnetic Nozzle by Using Fully Particle-In-Cell Code," *Journal of Physics: Conference Series*, Vol. 112, No. 4, 2008, pp. 1–4.
doi:10.1088/1742-6596/112/4/042082

[11] Harned, D. S., "Quasineutral Hybrid Simulation of Macroscopic Plasma Phenomena," *Journal of Computational Physics*, Vol. 47, No. 3, 1982, pp. 452–462.
doi:10.1016/0021-9991(82)90094-8

[12] Mankofsky, A., Sudan, R. N., and Denavit, J., "Hybrid Simulation of Ion Beams in Background Plasma," *Journal of Computational Physics*, Vol. 70, No. 1, 1987, pp. 89–116.
doi:10.1016/0021-9991(87)90003-9

[13] Horowitz, E. J., Shumaker, D. E., and Anderson, D. V., "QN3D: A Three-Dimensional Quasi-Neutral Hybrid Particle-in-Cell Code with Applications to the Tilt Mode Instability in Field Reversed Configurations," *Journal of Computational Physics*, Vol. 84, No. 2, 1989, pp. 279–310.
doi:10.1016/0021-9991(89)90234-9

[14] Maeno, A., Kajimura, Y., Sunahara, A., Yamamoto, N., Yasunaga, M., Hinaga, T., Hanaya, T., Fujioka, S., Johzaki, T., Mori, Y., and Nakashima, H., "Numerical Analysis of Magnetic Thrust Chamber System for Laser Fusion Rocket Considering the Creation Process of Laser-Produced Plasma," *Transactions of the Japan Society for Aeronautical and Space Sciences, Aerospace Technology Japan*, Vol. 10, No. 28, 2012, pp. 71–77.
doi:10.2322/tastj.10.Pb_71

[15] MacFarlane, J. J., Golovkin, I. E., and Woodruff, P. R., "HELIOS-CR—A 1-D Radiation-Magnetohydrodynamics Code with Inline Atomic Kinetics Modeling," *Journal of Quantitative Spectroscopy and Radiative Transfer*, Vol. 99, Nos. 1–3, 2006, pp. 381–397.
doi:10.1016/j.jqsrt.2005.05.031

[16] Sunahara, A., Nishihara, K., and Sasaki, A., "Optimization of Extreme Ultraviolet Emission from Laser-Produced Tin Plasmas Based on Radiation Hydrodynamics Simulations," *Journal of Plasma and Fusion Research*, Vol. 3, 2008, pp. 1–5.
doi:10.1585/pfr.3.043

[17] Lyon, S. P., and Johnson, J. D., "SESAME: The Los Alamos National Laboratory Equation of State Database," Los Alamos National Lab., LA-UR-92-3407, Los Alamos, NM, 1992, p. 1.

[18] Braginskii, S. I., "Transport Processes in a Plasma," *Reviews of Plasma Physics*, Vol. 1, Consultants Bureau, New York, 1965, pp. 250.

[19] Spitzer, L. Jr., and Härm, R., "Transport Phenomena in a Completely Ionized Gas," *Physical Review Letters*, Vol. 89, No. 5, 1953, pp. 977–981.
doi:10.1103/PhysRev.89.977

[20] Skupsky, S., "Coulomb Logarithm for Inverse-Bremsstrahlung Laser Absorption," *Physical Review A*, Vol. 36, No. 12, 1987, pp. 5701–5712.
doi:10.1103/PhysRevA.36.5701

[21] Malone, R. C., McCrory, R. L., and Morse, R. L., "Indications of Strongly Flux-Limited Electron Thermal Conduction in Laser-Target Experiments," *Physical Review Letters*, Vol. 34, 1975, pp. 721–724.
doi:10.1103/PhysRevLett.34.721

[22] Spitzer, L. Jr., *Physics of Fully Ionized Gases*, 2nd ed., Dover, New York, 2006, pp. 131–136.

[23] Langdon, A. B., "Nonlinear Inverse Bremsstrahlung and Heated-Electron Distributions," *Physical Review Letters*, Vol. 44, No. 9, 1980, pp. 575–579.
doi:10.1103/PhysRevLett.44.575

[24] Johnston, T. W., and Dawson, J. M., "Correct Values for High-Frequency Power Absorption by Inverse Bremsstrahlung in Plasmas" *Physics of Fluids*, Vol. 16, No. 5, 1973, p. 722.
doi:10.1063/1.1694419

[25] Kruer, W. L., *The Physics of Laser Plasma Interactions*, Westview Press, Boulder, Colorado, 2003, pp. 45–56.

[26] Minerbo, G. N., "Maximum Entropy Eddington Factors," *Journal of Quantitative Spectroscopy and Radiative Transfer*, Vol. 20, No. 16, 1978, pp. 541–545.
doi:10.1016/0022-4073(78)90024-9

[27] Birdsall, C. K., and Langdon, A. B., *Plasma Physics via Computer Simulation*, Taylor and Francis, New York, 2004, pp. 437–441, Appendix C.

[28] Pearlman, J. S., "Faraday Cups for Laser Plasmas," Review of Scientific Instruments, Vol. 48, No. 8, 1977, pp. 1064–1067.
doi:10.1063/1.1135184

[29] Minami, T., Funaki, I., Yamakawa, H., and Nakayama, Y., "Experimental Study of Magnetic Sails," ISAS Research Note 790, 2005.

G. Spanjers
Associate Editor